nature communications

Article

https://doi.org/10.1038/s41467-024-48690-7

General synthesis of ionic-electronic coupled two-dimensional materials

Received: 3 February 2024

Accepted: 10 May 2024

Xiang Xu[1,4], Yunxin Chen[1,4], Pengbin Liu[1], Hao Luo[2], Zexin Li[1], Dongyan Li[1], Haoyun Wang[1], Xingyu Song[1], Jinsong Wu[2], Xing Zhou[1] ✉ & Tianyou Zhai[1,3] ✉

Two-dimensional (2D) AMX_2 compounds are a family of mixed ionic and electronic conductors (where A is a monovalent metal ion, M is a trivalent metal, and X is a chalcogen) that offer a fascinating platform to explore intrinsic coupled ionic-electronic properties. However, the synthesis of 2D AMX_2 compounds remains challenging due to their multielement characteristics and various by-products. Here, we report a separated-precursor-supply chemical vapor deposition strategy to manipulate the chemical reactions and evaporation of precursors, facilitating the successful fabrication of 20 types of 2D AMX_2 flakes. Notably, a 10.4 nm-thick $AgCrS_2$ flake shows superionic behavior at room temperature, with an ionic conductivity of 192.8 mS/cm. Room temperature ferroelectricity and reconfigurable positive/negative photovoltaic currents have been observed in $CuScS_2$ flakes. This study not only provides an effective approach for the synthesis of multielement 2D materials with unique properties, but also lays the foundation for the exploration of 2D AMX_2 compounds in electronic, optoelectronic, and neuromorphic devices.

The coupled ionic-electronic effects in two-dimensional (2D) materials have attracted tremendous interest in recent years as they endow the materials with diverse responses to external stimuli, further facilitating the development of next-generation electronic, optoelectronic, and neuromorphic devices[1–5]. For example, the hybrid of the ionic gate with 2D materials enables the modulation of the phase transition[6–8] and band structures[9–11] in 2D materials due to the strong gate control ability of the ionic gate. Furthermore, the extrinsic ionic states can be introduced into 2D materials through the pre-treatment, such as the intercalation of external ions[4,12] and plasma treatment[5,13]. Subsequently, employing an electric field to control the migration of ions allows for emulating the function of biological neurons and synapses, showing the vast potential in the field of neuromorphic computing[4,5,13]. It should be noted that these additional modification techniques require complex processes and result in interface states[4,11], thereby impeding the exploration of novel physical and chemical properties, as well as hindering the development of high-density integrated devices. The intrinsic ionic-electronic coupled 2D materials are expected to solve the above problems.

AMX_2 is a family of mixed ionic-electronic conductors (where A is a monovalent metal ion, M is a trivalent transition or main group metal, and X is a chalcogen). The monovalent metal ions Cu^+ and Ag^+ have 3d-orbital electrons that exhibit second-order Jahn-Teller effect[14], and normally possess a low ion migration barrier[15]. Thus, introducing the superionic conductivity[16–18], multiferroics[19,20], and magnetism[21] properties within the AMX_2. Meanwhile, the multielement characteristic and various atomic structures give the AMX_2 rich band structures[19,22,23], making the AMX_2 compounds excellent systems for studying intrinsic coupled ionic-electronic properties. While a few demonstrations of the synthesis of 2D AMX_2 have been reported[16,24], the fabrication of most of these compounds remains elusive, hindering their exploration and application. Chemical vapor deposition (CVD) has been widely used in

---

[1]State Key Laboratory of Materials Processing and Die & Mould Technology, School of Materials Science and Engineering, Huazhong University of Science and Technology, Wuhan 430074, P. R. China. [2]Nanostructure Research Center, State Key Laboratory of Advanced Technology for Materials Synthesis and Processing, Wuhan University of Technology, Wuhan 430070, P. R. China. [3]Optics Valley Laboratory, Hubei 430074, P. R. China. [4]These authors contributed equally: Xiang Xu, Yunxin Chen. ✉e-mail: zhoux0903@hust.edu.cn; zhaity@hust.edu.cn

the synthesis of 2D materials[25–34]. For the synthesis of multielement compounds like AMX_2, three kinds of precursors are required. In the common CVD process, the metal and chalcogen precursors transport along the same path, leading to uncontrollable pre-reactions and an unstable supply of precursors, thereby hindering the controllable synthesis of 2D AMX_2.

In this work, we demonstrate a separated-precursor-supply strategy in which the suppressed by-reactions and controllable supply of precursors ensure the general synthesis of 20 distinct 2D AMX_2, 18 types of which have never been reported. Interestingly, the as-grown AMX_2 flakes exhibit unique electronic and ionic properties. A 10.4 nm $AgCrS_2$ flake shows superionic conductor characteristics at room temperature with an ionic conductivity of up to 192.8 mS/cm. The as-grown $CuScS_2$ flakes exhibit semiconductor ferroelectric properties, and show a Curie temperature reaching ~370 K. Notably, the reconfigurable positive/negative photovoltaic current can be observed in $CuScS_2$ devices due to the adjustable ion migration drived by the external electric field. This work not only provides an effective strategy for synthesizing multielement 2D materials but also opens up opportunities for studying the properties and potential applications of a wide variety of 2D AMX_2.

Results and discussion

General growth and characterization of AMX_2

We first discuss the difficulties of controllable synthesis 2D AMX_2. For multielement compounds like AMX_2, during the CVD process, there are many possible reactions between metal and chalcogen precursors (Supplementary Fig. 1). And the formation energy of most binary products is less than that of AMX_2 (Fig. 1a)[35]. Even if the AMX_2 is more favorable thermodynamically, it is hard to control the

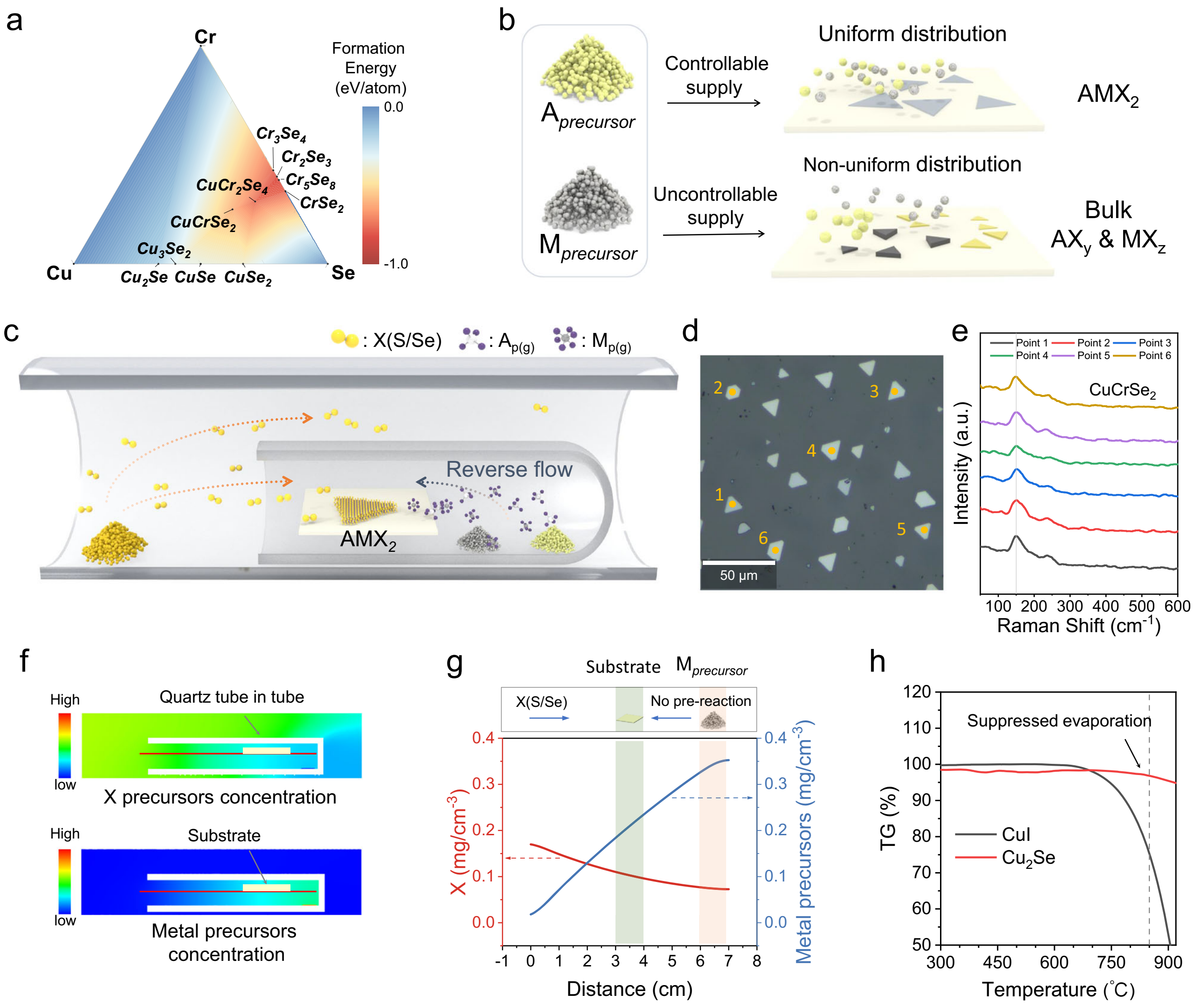

Fig. 1 | Synthesis mechanism of chemical vapor deposition (CVD) growth AMX_2. **a** The formation energy of $CuCrSe_2$ phase diagram[35]. **b** The kinetic growth process is influenced by the supply of metal precursors. A and M present the two kinds of metal elements of AMX_2 compounds, and X represents the chalcogen element. The x and y in the AX_y and MX_z demonstrate the possible stoichiometric ratio of the binary by-products in the (**a**) (such as CuSe, Cu_2Se, etc.). **c** Schematic image of the CVD setup. The orange and blue dash arrows represent the transportation paths of the vapored chalcogen precursor and metal precursors ($A_{p(g)}$ and $M_{p(g)}$), respectively. **d** The large area optical image of the as-synthesized $CuCrSe_2$ nanosheets. **e** The Raman spectra of the flakes in the (**d**). The vertical dash line located at 150 cm^{-1} demonstrates the consistent Raman peaks of the as-synthesized $CuCrSe_2$ nanosheets. **f** The computational fluid dynamics (CFD) simulated distribution of X (S/Se) and metal precursors concentration. **g** The CFD simulated variation curve of precursor concentration along the red line in the (**f**). The green and pink shaded areas schematically represent the position of the substrate and metal precursors, respectively. **h** Thermogravimetric analysis (TGA) of CuI and Cu_2Se powders. The black and red curves correspond to the weight-loss curves of CuI and Cu_2Se, respectively. The vertical dash line located at 850°C demonstrates that the evaporation of excessively selenated metal precursors will be significantly suppressed.

reactions of precursors during transportation due to the premixing of the vaporized precursors in common CVD, which promotes the non-uniform distribution of precursors and results in undesired products (Fig. 1b). Taking the synthesis of $CuCrSe_2$ as an example since other AMX_2 compounds have similar troubles. In the common CVD process, the Se vapor will pass by the Cu and Cr precursors before reaching the substrate, resulting in uncontrollable pre-reactions (Supplementary Fig. 2). Due to the consistent exposure of the metal source to the Se vapor, the metal precursor powders undergo excessive selenization (Supplementary Fig. 3a), which will suppress the vaporization and destabilize the precursor supply, then giving rise to a large number of by-products such as Cu_xSe on the substrate (Supplementary Fig. 3b, c), hindering the controlled synthesis of AMX_2.

To achieve the controllable synthesis of 2D AMX_2 compounds, it is imperative to suppress undesired by-reactions. We have approached this challenge from a kinetic perspective. Specifically, we report a separated-precursor-supply strategy to suppress the by-reactions during mass transportation. The schematic representation of the CVD setup can be found in Fig. 1c and Supplementary Fig. 4a. First, stable source feeding of chalcogen is important. Here, we placed the resolidified chalcogen source, which is believed to realize stable source feeding and further reduce chalcogen vacancy forming in the CVD process[36], at the upstream. More importantly, we should ensure the temporal and spatial uniform supply of two metal precursors to support the synthesis of 2D AMX_2, which is much more difficult than the synthesis of binary compounds. We placed two kinds of metal precursors at the bottom of a one-side-sealed quartz tube, then the small quartz tube was placed downstream of the furnace tube (see Methods for more details). In this system, the transport process of metal precursors is protected by the small quartz tube and is separated from the transport process of chalcogen vapor (Supplementary Fig. 4b). Based on this method, we realized the uniform synthesis of the 2D AMX_2 materials (Fig. 1d, e).

Computational fluid dynamics (CFD) simulations predict that the gas flow inside the small quartz tube is primarily directed towards the open side, opposing the flow direction of carrier gas, and exhibits significantly lower velocity compared to the external gas flow outside the small tube (Supplementary Fig. 6). This results in a reverse mass flow opposite to the Se precursor's transport direction (Supplementary Figs. 6 and 7). As a consequence, the concentration of metal precursor vapors is lower at the tube's open side and higher at the tube's sealed side, and the Se vapors' concentration distribution is opposite to that of the metal precursor vapor (Fig. 1f, g). The relatively high concentration of the metal precursor vapor in the small tube prevents excessive selenization of the metal precursor powder, ensuring the stable vaporization of the metal precursor during the whole CVD process. In contrast, without the confinement of the small quartz tube, the vapor of the metal precursor and Se precursor meet before reaching the substrate (Supplementary Fig. 8) which will facilitate the occurrence of by-reactions. And the concentration of chalcogen precursor is much higher than the metal precursors. This will result in excessive selenization or sulfurization, making the supply of metal precursor unstable (Fig. 1h). However, when the metal precursor is confined within the small quartz tube, its concentration is one order of magnitude higher compared to the situation without spatial confinement (Supplementary Fig. 9). The ample metal precursor supply, which matches the supply of chalcogen precursor, greatly suppress phase separation.

Taking the synthesis of 2D $CuCrSe_2$ as an example again. Different from the common CVD, the separated-precursor-supply strategy protected the metal precursors from excessive selenization and suppressed the pre-reactions between the Cu/Cr precursors and Se precursors (Supplementary Fig. 10), thereby ensuring a stable supply of metal precursors and suppressing undesired by-products. Through this approach, 2D $CuCrSe_2$ with consistent phase and uniform morphology can be obtained (Fig. 1d, e). Figure 2 shows a summary of optical images of the 20 kinds of 2D AMX_2 materials prepared using this method. The corresponding synthesis conditions are described in the Methods, more details are summarized in Supplementary Table 1 and Supplementary Methods. To our best knowledge, 18 of them have not been previously synthesized using CVD or mechanical exfoliation methods (Supplementary Table 2). The synthesized AMX_2 compounds are mainly selenides and sulfides and contain 9 metal elements including two monovalent metal ions (Cu^+, Ag^+); three transition metals (Sc, Cr, Fe); and four main group metals (Ga, In, Sb, Bi). To show our uniform growth, the larger area optical images with more flakes are shown in Supplementary Fig. 11. Most of the synthesized 2D AMX_2 compounds exhibit triangular or hexagonal shapes, and a small fraction shows rhombic or nanoribbon morphologies. The thickness of most samples can be reduced to below 10 nm, and some can even reach few unit-cell thickness, such as $CuCrS_2$ (2.56 nm), $AgCrSe_2$ (1.86 nm), $CuFeSe_2$ (1.9 nm), and $CuSbS_2$ (0.79 nm) (Supplementary Fig. 12), which demonstrates the effectivity and generality of our growth methods.

To elucidate the structural features of AMX_2 compounds, we conducted high-angle annular dark-field scanning transmission electron microscopy (HAADF-STEM) characterization on three representative materials, namely $AgCrS_2$ with $R3m$ space group, $AgBiSe_2$ with $R\bar{3}m$ space group, and $CuInS_2$ with $I\bar{4}2d$ space group. For the as-grown $AgCrS_2$. The High-resolution transmission electron microscopy (HRTEM) image along the [001] crystal direction reveals its hexagonal atomic arrangement, with a measured lattice spacing of $d(2\bar{1}0) = 1.71$ Å (Fig. 3a). The cross-sectional HAADF-STEM image along the [100] crystal direction is shown in Fig. 3b, with a measured lattice spacing of $d(003) = 6.83$ Å. Based on the layered characteristics, the structure can be understood as alternating stacking of CrS_2 layers and Ag^+ ion layers along the c-axis. The brightness variation of the dashed line in Fig. 3b is depicted in Fig. 3c, where Ag exhibits the highest brightness, followed by Cr with intermediate brightness, and S appears the darkest. The 3d orbital electrons of Cr^{3+} in the material hybridize with the p orbital electrons of S, forming $[CrS_6]$ octahedral coordination structure (shown at the blue quadrilateral position in Fig. 3b). The $[CrS_6]$ octahedra are edge-connected to form the CrS_2 layer (Supplementary Fig. 13). Meanwhile, Ag^+ ions orderly occupy the tetrahedral sites between the CrS_2 layers (shown at the red triangular position in Fig. 3b). This ordered tetrahedral occupancy results in the breaking of inversion symmetry, leading the material to exhibit a pronounced optical second harmonic generation (SHG) response (Supplementary Fig. 14g). Similarly, $AgBiSe_2$ also exhibits typical layered structure characteristics, with Ag^+ confined between the $BiSe_2$ layers. The HRTEM image along the [001] crystal direction also demonstrates the characteristic hexagonal atomic arrangement, with a measured lattice spacing of $d(2\bar{1}0) = 2.07$ Å (Fig. 3d). However, different with the $AgCrS_2$, the Ag^+ ions in the $AgBiSe_2$ occupy the octahedral sites between the $BiSe_2$ layers (shown at the red quadrilateral in Fig. 3e), with a measured lattice spacing of $d(003) = 6.77$ Å. The structure of $CuInS_2$ is composed of $[CuS_4]$ and $[InS_4]$ tetrahedra. The exposed surface of the sample has a hexagonal atomic arrangement, namely the (112) plane (Fig. 3g). From HRTEM images and selected area electron diffraction (SAED) patterns, the annotated lattice spacings are $d(20\bar{4}) = 1.96$ Å and $d(112) = 3.26$ Å, respectively. The measured crystal plane spacings for these three materials are consistent with previous reports. Additionally, we provided Raman spectra, photoluminescence spectra, and optical SHG response for each sample (Supplementary Figs. 14–18), and we conducted HRTEM and energy-dispersive spectroscopy (EDS) to characterize the 20 kinds of as-grown AMX_2 compounds (Supplementary Figs. 19–38). The synthesized AMX_2 compounds exhibit good agreement with the expected phases and show high crystalline quality.

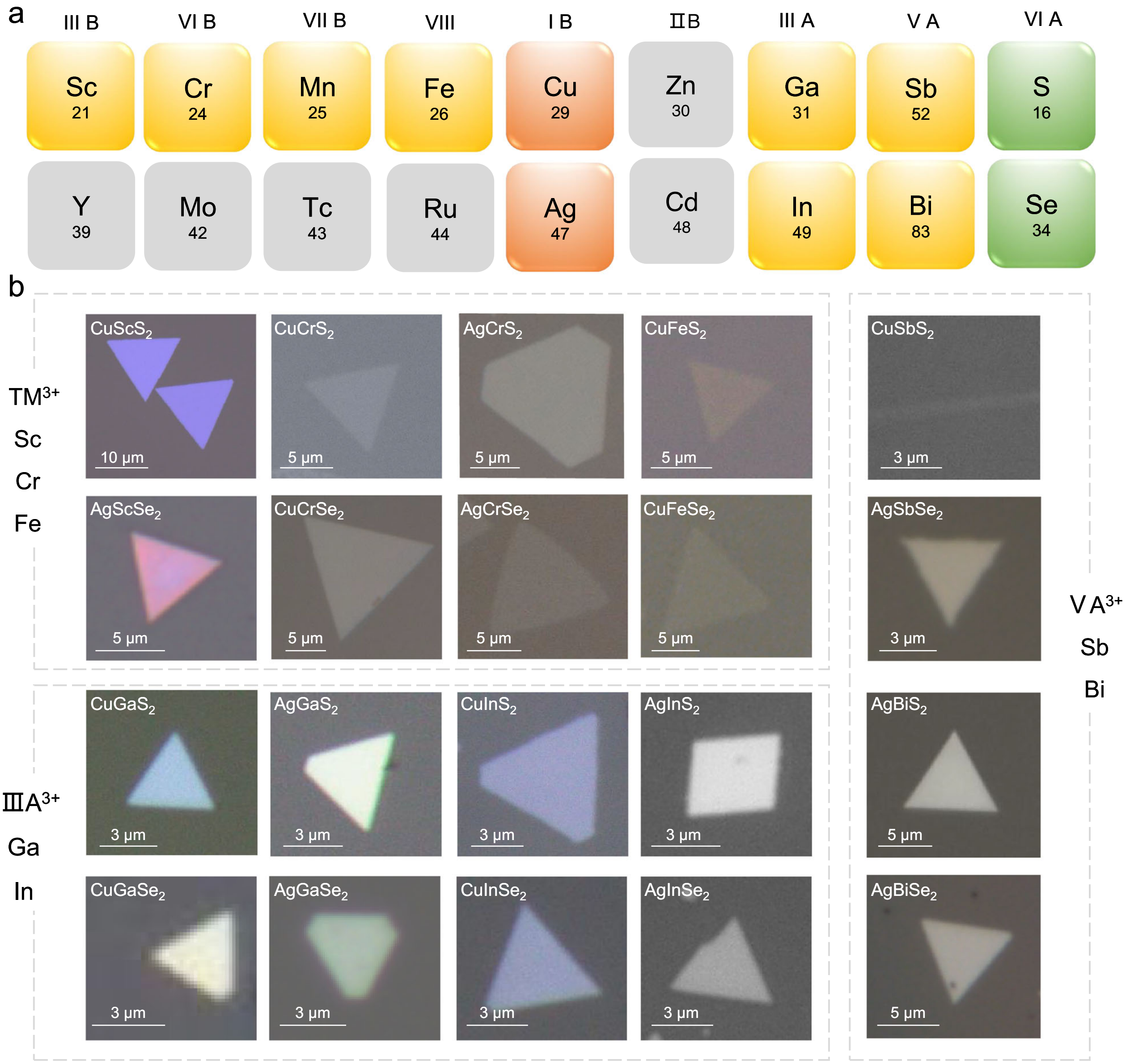

Fig. 2 | Optical microscopy images of the 20 kinds of as-synthesized 2D AMX_2 compounds. **a** Summary of 2D AMX_2 compounds that can be synthesized using this method. Orange, element A; yellow, element M; green, element X. **b** Optical images of the as-synthesized 2D AMX_2 nanosheets.

In summary, the as-grown AMX_2 compounds typically possess a quasi-2D layered structure, where monovalent metal ions Cu^+ and Ag^+, known for their strong migration characteristics[17,18], are confined within the interlayer space of MX_2 (Supplementary Fig. 13). This means that most AMX_2 materials possess inherent migratable ions, and have natural 2D ion migration pathways. As a result, AMX_2 materials exhibit intrinsic ion characteristics[18,23,37]. Additionally, the 3d orbital electrons of the transition metal in the MX_2 layers may introduce ferromagnetic or antiferromagnetic characteristics to the materials[19,20,38] (Supplementary Table 3). In addition to their layered structure characteristics, 14 kinds of the as-grown 2D AMX_2 possess features with broken inversion symmetry (Supplementary Table 4), endowing them with optical SHG properties, as well as piezoelectric and ferroelectric properties[24,39].

The ionic and electronic properties of AMX_2 compounds

Building upon the structural attributes of AMX_2, Cu^+/Ag^+ ions can undergo hopping between the tetrahedral or octahedral sites within the MX_2 interlayer space when the temperature is higher than a certain point[18,37]. Simultaneously, under the influence of an external electric field, ions can exhibit directed migration, thereby manifesting superionic conductor features[16,40] (Fig. 4a). We commence our investigation by delving into the ionic migration properties of AMX_2, using $AgCrS_2$ as an illustrative example, we fabricated two-terminal electrode devices and employed Au as a blocking electrode for testing ion conductivity. The impedance spectra of samples with different thicknesses (Fig. 4b) can all be fitted with two semicircles. These curves exhibit characteristic mixed ion-electron conductivity features[16,23]. According to the equivalent circuit of the mixed ionic-electronic conductor model (illustrated in the inset of Fig. 4b), ionic conductivity can be obtained by fitting the electrochemical impedance curves, and the detail of the fitting process is described in Methods and Supplementary Fig. 39. In a 10.4 nm $AgCrS_2$ nanosheet, we measured an ionic conductivity of 192.8 mS/cm. Interestingly, we observed that the ionic conductivity increases as the sample thickness decreases (Supplementary Fig. 40). This trend is consistent with the previous report on $AgCrS_2$ samples obtained via electrochemical exfoliation[16]. However, our samples exhibit a higher ionic conductivity, which could be attributed to the superior crystalline quality resulting from our

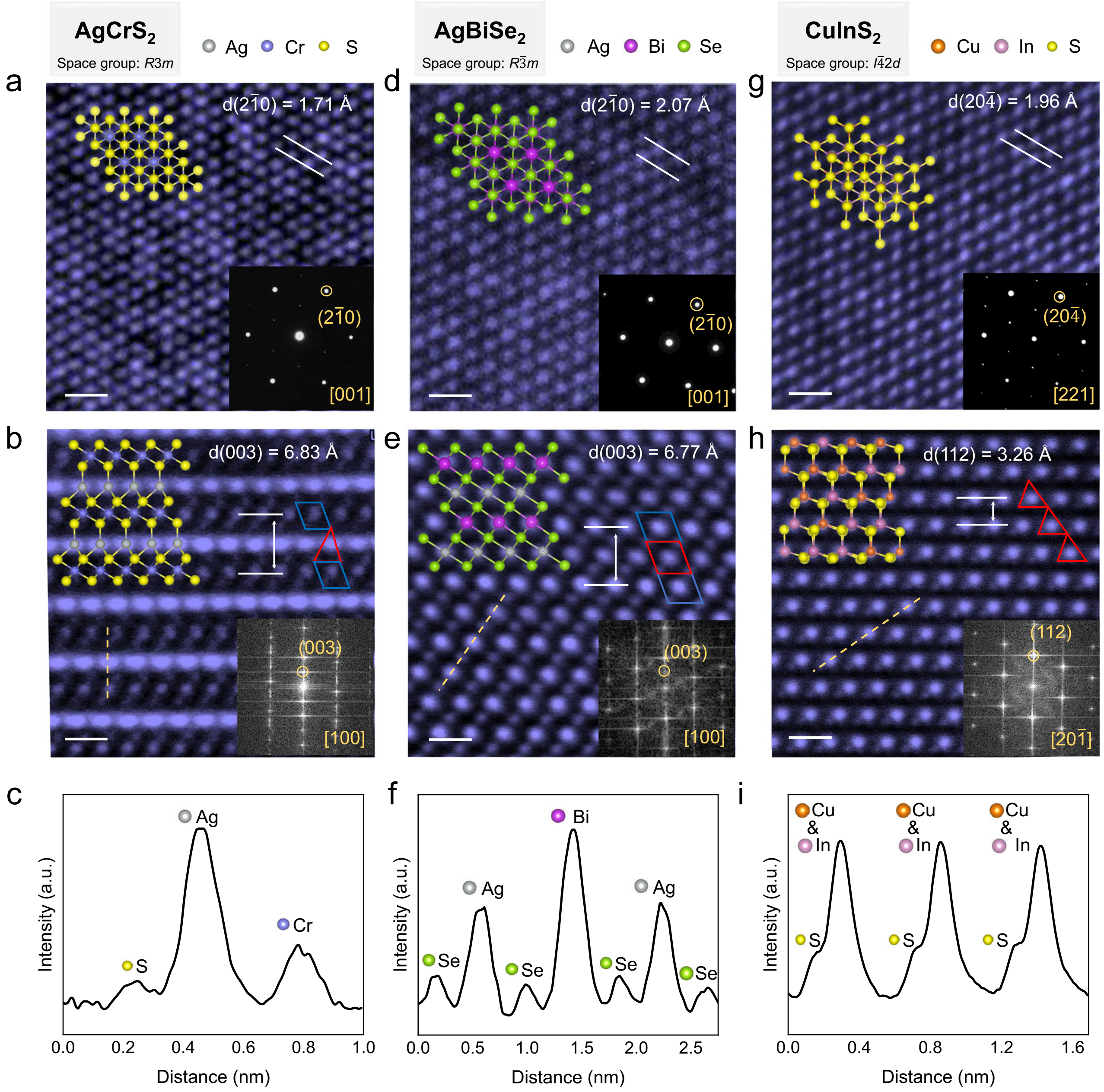

Fig. 3 | Structural analysis of selected three as-synthesized 2D AMX_2 compounds. a, d, g High-resolution transmission electron microscopy (HRTEM) images of $AgCrS_2$, $AgBiSe_2$, and $CuInS_2$ along the direction out of the plane of the as-grown nanosheets, scale bar: 0.5 nm. The insets display the top view of atomic structure models and selected area electron diffraction (SAED) patterns. **b**, **e**, **h** Cross-sectional high-angle annular dark-field scanning transmission electron microscopy (HAADF-STEM) images of $AgCrS_2$, $AgBiSe_2$, and $CuInS_2$, scale bar: 0.5 nm. The insets display the side view of the atomic structure models and the fast Fourier transform (FFT) patterns. The blue and red polygons represent the octahedral and tetrahedron sites. **c**, **f**, **i** Intensity profiles of the orange dash lines in (**b**), (**e**), and (**h**).

synthesis method. Compared to other ion conductors, the ionic conductivity of the $AgCrS_2$ nanosheets synthesized by us remains at a relatively high level (Fig. 4c)[16,40–46].

Cu^+/Ag^+ ions can not only undergo long-distance migration but also experience local displacements, giving rise to ferroelectricity, specifically ion displacement-induced ferroelectricity[47]. By applying a vertical electric field, we can drive ion displacements between the two enantiomeric tetrahedral sites within the MX_2 interlayer space, resulting in spontaneous polarization reversal and exhibiting ferroelectric properties (Fig. 4d). Taking $CuScS_2$ as an example. The SHG mapping shows the uniform non-centrosymmetric crystal structure and the single domain characteristics of the as-synthesized $CuScS_2$ flake (Supplementary Fig. 41). Then, we employed piezoresponse force microscopy (PFM) testing methods to investigate the material's room-temperature ferroelectric properties. The as-grown $CuScS_2$ flakes exhibited distinct ferroelectric phase hysteresis loops and typical amplitude butterfly curves (Fig. 4e). Simultaneously, we performed domain read-write operations on the flakes. The PFM phase image shows two stable opposite polarization domain regions (the inset of Fig. 4e), validating the out-of-plane ferroelectric properties of $CuScS_2$ at room temperature. We also tried to reveal the in-plane (IP) polarization of the $CuScS_2$ flakes. However, there is no typical IP PFM phase and amplitude hysteresis loop (as Supplementary Fig. 42 shows), suggesting no IP polarization in the as-synthesized $CuScS_2$ flakes. Furthermore, to reveal the temperature stability of the ionic displacement-type ferroelectricity in $CuScS_2$, which is critical to the applications, we employed high-temperature SHG measurements to characterize its ferroelectric Curie temperature (T_C). As the

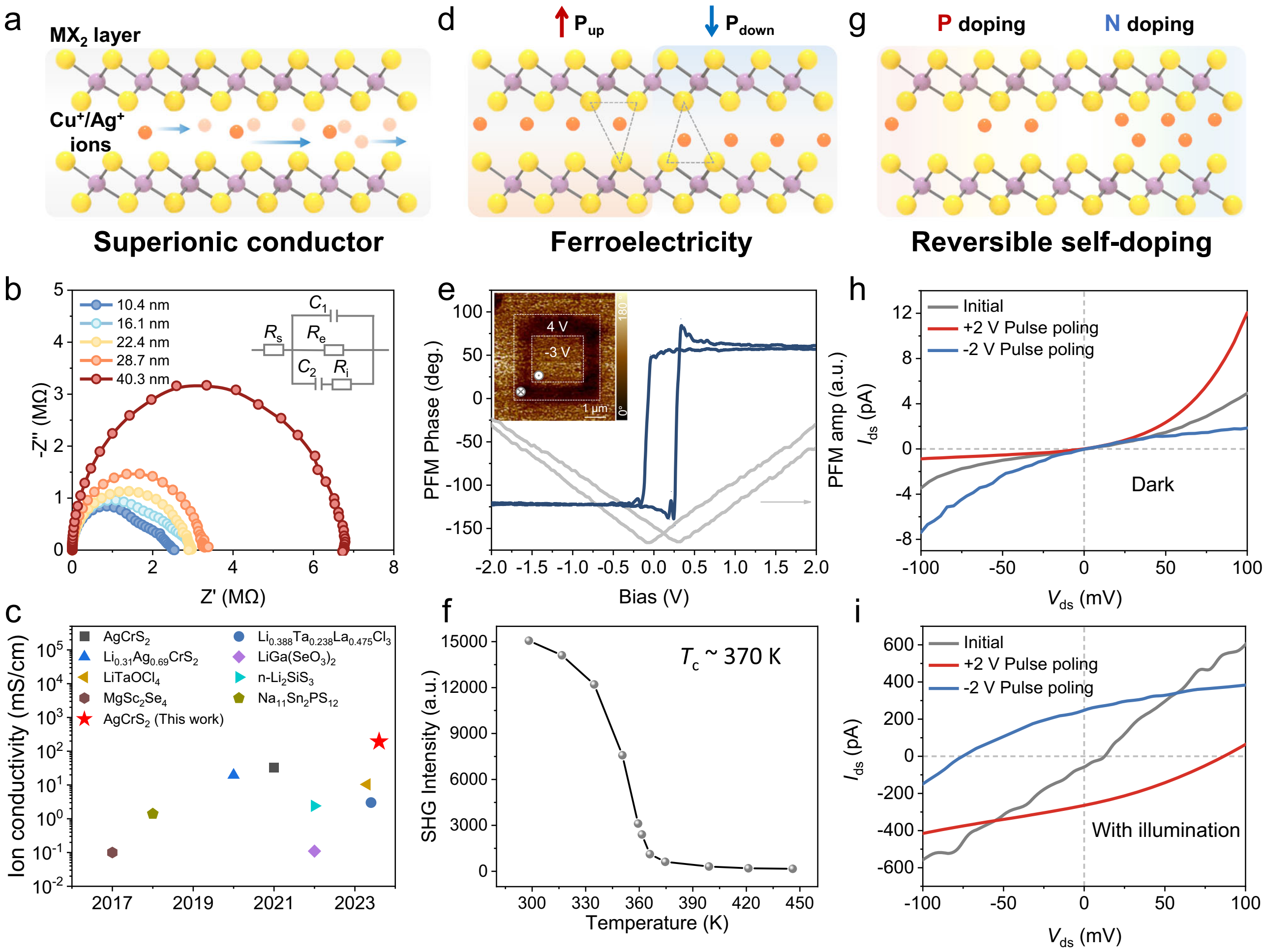

Fig. 4 | The ionic and electronic properties of two representative as-synthesized 2D AMX_2 compounds. a, **d**, **g** Schematic diagrams of the superionic conductor (**a**), ferroelectricity (**d**), and reversible self-doping (**g**) properties that arise from the ionic-electronic coupling effects. The blue arrows in (**a**) present the directed long-distance migration of the Cu^+/Ag^+ ions within the interlayer. The dashed triangles in (**d**) show the two enantiomeric tetrahedral sites of Cu^+/Ag^+ ions, corresponding to the up and down ferroelectric polarization states of the materials. **b** The impedance spectroscopic measurement for $AgCrS_2$ nanosheets with different thicknesses. The inset shows the equivalent circuit, where R_s, R_e, and R_i correspond to the contact resistance, electronic resistance, and ionic resistance, respectively, and C_1 and C_2 are the constant phase elements. The detailed calculation process of ionic conductivity is shown in Supplementary Fig. 39. **c** The comparison of ionic conductivity with other reported superionic conductors[16,40–46]. **e** Piezoresponse force microscopy (PFM) phase and amplitude hysteresis loop of $CuScS_2$ nanosheet, the inset is the ferroelectric domains (white dashed square area) after forward and reverse DC bias polarization. The out-of-plane arrow symbols represent the $\mathbf{P}_{\mathrm{up}}$ and $\mathbf{P}_{\mathrm{down}}$ states of the nanosheet after polarization. **f** Temperature-dependent optical second harmonic generation (SHG) measurement of a $CuScS_2$ nanosheet, demonstrating a ferroelectric Curie temperature (T_c) of ~ 370 K. **h**, **i** Memristor behavior (**h**) and switchable photovoltaic behavior under illumination (λ = 532 nm, 256.6 mW/cm^2) (**i**) after positive/negative pulse polarization of the $CuScS_2$-based device.

temperature increases to above 370 K, the SHG signal of $CuScS_2$ nearly quenches (Fig. 4f and Supplementary Fig. 43a), indicating the disruption of the ordered occupancy of Cu^+ ions in the interlayer tetrahedral positions (Supplementary Fig. 43b). This implies that the T_C of $CuScS_2$ is approximately 370 K, demonstrating significant potential for extensive applications in the field of ferroelectricity.

The movement of ions within the material often results in concentration gradients, leading to different doping effects[48]. By employing electrical pulses to control the migration of ions within the material, reversible self-doping characteristics can be achieved (Fig. 4g), consequently leading to interesting electrical and optoelectronic properties, which is exemplified by 2D $CuScS_2$. First-principles calculations predict that the migration barrier for a Cu^+ ion to move through the tetrahedral-octahedral-tetrahedral path within the $CuScS_2$ is 0.24 eV (Supplementary Fig. 44). Such a low migration energy barrier is comparable to that for intercalated Li^+ ions in transition metal dichalcogenides (TMDs)[49], indicating that a relatively small external electric field is sufficient to drive the migration of Cu^+ ions. Applying electric pulses for polarization is an effective approach for achieving controlled migration of interlayer ions as we can modulate the pulse width and amplitude precisely[50]. Firstly, we investigated the ionic-electronic coupled properties of $CuScS_2$-based devices under dark conditions using triangular electric pulses (Supplementary Fig. 45a). As shown in Fig. 4h, the initial state *I-V* curve of the device is symmetric in the positive and negative voltage ranges. After poling the device with a forward bias pulse, the *I-V* curve exhibits characteristic diode-like behavior, indicating the generation of a potential barrier within the device under the influence of the electric pulse. Furthermore, upon applying a reverse bias pulse, the rectification direction of the device is reversed, indicating that the direction of internal potential barriers within the material can be modulated by the electric pulse. This reconfigurable potential barrier allows for continuous modulation of the device resistance through electric pulses, enabling memristive functionality (Supplementary Fig. 45b–d). Under illumination, compared to the initial state, the device exhibits a noticeable photovoltaic response after poling by 2 V/0.5 s electric pulse. The device demonstrates a photovoltaic short-circuit current (I_{sc}) of ~270 pA when the source-drain bias voltage (V_{ds}) is zero and shows a distinct open-circuit voltage (V_{oc}) of ~85 mV. Similar to the dark situation, the photovoltaic response direction also reverses after the device undergoes reverse poling electric pulses (Fig. 4i). This reconfigurable photovoltaic response exhibits great stability during *I-t* testing (Supplementary Fig. 46). To reveal the mechanism of this reconfigurable photovoltaic response, we firstly analyzed the possible bulk photovoltaic effect (BPVE) in the ferroelectric $CuScS_2$. Based on the single-domain characteristic of as-synthesized $CuScS_2$ (Supplementary Fig. 41), the BPVE would induce obvious I_{sc} at the initial-state device. However, the I_{sc} of the initial-state device is ignorable (Fig. 4i), demonstrating that the BPVE is negligible here. Moreover, the undetectable IP ferroelectricity of the as-synthesized $CuScS_2$ also proves this point. Then, we consider that the long-distance migration of the Cu^+ ions could induce reversible self-doping, which also can give rise to the reconfigurable photovoltaic response. Thus, we conducted cross-sectional EDS scanning tests on the polarized devices and observed that the distribution of Sc and S elements in the material remains uniformly distributed. However, the content of Cu elements beneath the electrode is significantly higher than in the channel region (Supplementary Fig. 47). This confirms the migration of Cu^+ ions after poling by the electric pulse. Moreover, the first-principles calculations indicate that the local absence or accumulation of Cu^+ ions resulting from ion migration will introduce significant p-type or n-type doping in the material (Supplementary Fig. 48), which is similar to the doping effect of point defects[5]. This coupling effect between ion migration and charge doping induces the emergence of the modulated potential barrier within 2D $CuScS_2$ and finally gives rise to the memristive behavior and reconfigurable photovoltaic response, which is crucial to the logic and neuromorphic devices[5,51].

In summary, we have demonstrated a separated-precursor-supply CVD method to control the reactions and vaporization of precursors. 20 kinds of 2D AMX_2 compounds have been synthesized successfully showing the practicality of our approach. Detailed structural analysis and comprehensive characterization have revealed the high crystalline quality of the prepared AMX_2 materials. Notably, the as-grown 2D AMX_2 flakes show intriguing ionic and electronic properties. A high ionic conductivity of 192.8 mS/cm can be observed in a 10.4 nm $AgCrS_2$ flake at room temperature. The synthesized 2D $CuScS_2$ flakes show ion displacement-induced ferroelectricity at room temperature. Meanwhile, the reconfigurable photovoltaic response based on the coupling of ions migration and charge doping also can be observed in $CuScS_2$. The achievement of generally synthesizing 2D AMX_2 compounds offers new insights into the vapor-phase synthesis of multielement 2D materials and provides an excellent material choice for exploration in electronics, optoelectronics, and neuromorphics.

Methods

CVD growth

2D AMX_2 compounds were synthesized by separated-precursor-supply CVD. Ultrahigh purity Ar (purity 99.999%) and H_2 (purity 99.999%) were used as the carrier gases. All the raw precursors were bought from Alfa Aesar with a purity higher than 99%. Freshly exfoliated mica was chosen as the growth substrate. A single temperature zone tube furnace (diameter, one inch) was used as the reaction instrument with a heating zone length of ~30 cm (Supplementary Fig. 5). A porcelain boat containing chalcogen precursor was placed upstream and heated to 150°C for sulfur (300°C for selenium). Two metal precursors were placed at the bottom of a one-side sealed small quartz tube with a length of 7 cm and a diameter of 10 mm. The growth substrate was placed in the small quartz tube too, 0.5-4 cm away from the metal precursors. Then, the small quartz tube was put downstream of the tube furnace and followed by the heating process. The heating rate is 50°C/min or 30°C/min for different AMX_2, and the reactions were carried out at 1 atm pressure. The schematic image of the CVD setup can be seen in Fig. 1c and Supplementary Fig 4a. The detailed growth parameters and descriptions are shown in Supplementary Table 1 and Supplementary Methods. The detailed characterizations of the morphology, phase, and atomic structures of as-synthesized ultrathin 2D AMX_2 are shown in Supplementary Figs. 11, 12, 14–38.

CFD simulations

To reveal the mass flow during the experiment, we did the numerical finite element simulation. During the modeling, we followed the real experiment setup of the tube furnace, the details can be seen in Supplementary Fig. 5. The transient model is used to simulate the real CVD process. The gravity and convection heat transfer were considered. Argon and air are considered ideal gases. The shear stress transfer (SST) model is used here. It is a low Reynolds number and comprehensive turbulence model, which can give more accurate near-wall results[52]. Firstly, we conduct a steady analysis of the system. Similar to the real condition of the heating process of the furnace, we assume the system is stable when the temperature of the monitor point reaches the goal point and does not change again. Based on this result, the transient analysis was conducted to reveal the mass transportation process of two precursors.

TG-DSC

TG-DSC testing was conducted using a DIAMOND TG/DTA thermal analyzer. Approximately 5 mg of the sample was added to an alumina crucible and heated from 20 °C to 900 °C at a rate of 50 K per minute in a pure argon atmosphere.

Characterizations

The morphologies of the as-grown AMX_2 nanosheets were characterized by an optical microscope (BX51, OLYMPUS) and atomic force microscope (Dimension icon, Bruker). Raman, photoluminescence, and SHG spectra were obtained by a confocal Raman system (Alpha 300 R, WITec) equipped with a 532 nm CW laser and a high-temperature test chamber (TS1000EV, Linkam). Femtosecond laser (Verdi, Coherent) was applied as the excitation source of SHG measurement. For the cross-sectional HAADF-STEM and EDS measurements, the samples were prepared by focus ion beam (Helios NanoLab G3 UC, FEI). The atomic resolution HAADF-STEM images were obtained by a double CS-corrected transmission electron microscopy (Titan Themis G2 60-300, FEI). For the TEM measurements, the samples were prepared with a poly (methyl methacrylate) (PMMA) assisted transfer method. TEM, SAED, and EDS were performed on an FEI Tecnai G2 F30 instrument.

Impedance spectra measurements

$AgCrS_2$ nanosheets were transferred to the silica substrate. Then, the Au/$AgCrS_2$/Au devices were fabricated by electron-beam lithography (EBL, FEI Quanta 650 SEM & Raith Elphy Plus) and thermal evaporation coating (Angstrom Engineering, Nexdep). The ionic conductivity of $AgCrS_2$ nanosheets is obtained by fitting the electrochemical impedance spectra (Autolab PGSTAT 302 N) of the Au/$AgCrS_2$/Ag devices at room temperature. The testing frequency range is 1 Hz to 1 MHz. To avoid electromagnetic interference the whole process was operated in a Faraday cage.

PFM measurements

The PFM measurements were conducted on the AFM platform (Dimension icon, Bruker). $CuScS_2$ nanosheets were transferred to the silica substrate that was covered with gold. A DC voltage was applied to the conductive tip coated with Pt/Ir to reverse the ferroelectric domain of the sample.

Device fabricating and electrical measurements

All the devices were transferred on the silicon substrate with a 300-nm-thick oxide film using a PMMA-assisted method. The Bi/Au was chosen to be the contact electrode. The electrical measurements were carried out with a semiconductor characterization system (4200SCS, Keithley) and a cryogenic probe station (CRX-6.5, Lake Shore).

Theory calculations

The present first principle DFT calculations are performed by Vienna Ab initio Simulation Package (VASP)[53] with the projector augmented wave (PAW) method[54]. The exchange-functional is treated using the generalized gradient approximation (GGA) of Perdew-Burke-Ernzerhof (PBE)[55] functional. The energy cutoff for the plane wave basis expansion was set to 450 eV and the force on each atom less than 0.02 eV/Å was set for the convergence criterion of geometry relaxation. The Brillouin zone integration is performed using $5 \times 5 \times 5$ and $9 \times 9 \times 9$ k-point sampling for structure optimization and electronic structure calculation, respectively. The self-consistent calculations apply a convergence energy threshold of 10^{-5} eV. Transition state searching was performed using the climbing-image nudged elastic band (CI-NEB) method[56].

Data availability

The data that support the plots within this paper and other findings of this study are available from the corresponding authors upon request.

References

1. Sangwan, V. K. & Hersam, M. C. Neuromorphic nanoelectronic materials. *Nat. Nanotechnol.* **15**, 517–528 (2020).
2. Fuller, E. J. et al. Parallel programming of an ionic floating-gate memory array for scalable neuromorphic computing. *Science* **364**, 6 (2019).
3. Liu, C. et al. Two-dimensional materials for next-generation computing technologies. *Nat. Nanotechnol.* **15**, 545–557 (2020).
4. Zhu, X., Li, D., Liang, X. & Lu, W. D. Ionic modulation and ionic coupling effects in MoS_2 devices for neuromorphic computing. *Nat. Mater.* **18**, 141–148 (2019).
5. Li, T. et al. Reconfigurable, non-volatile neuromorphic photovoltaics. *Nat. Nanotechnol.* **18**, 1303–1310 (2023).
6. Wu, Y., Li, D., Wu, C.-L., Hwang, H. Y. & Cui, Y. Electrostatic gating and intercalation in 2D materials. *Nat. Rev. Mater.* **8**, 41–53 (2022).
7. Li, L. J. et al. Controlling many-body states by the electric-field effect in a two-dimensional material. *Nature* **529**, 185–189 (2016).
8. Wu, C.-L. et al. Gate-induced metal–insulator transition in MoS_2 by solid superionic conductor LaF_3. *Nano Lett.* **18**, 2387–2392 (2018).
9. Alam, M. H. et al. Lithium-ion electrolytic substrates for sub-1V high-performance transition metal dichalcogenide transistors and amplifiers. *Nat. Commun.* **11**, 3203 (2020).
10. Domaretskiy, D. et al. Quenching the bandgap of two-dimensional semiconductors with a perpendicular electric field. *Nat. Nanotechnol.* **17**, 1078–1083 (2022).
11. Lee, S.-J. et al. Programmable devices based on reversible solid-state doping of two-dimensional semiconductors with superionic silver iodide. *Nat. Electron.* **3**, 630–637 (2020).
12. Edwards, B. et al. Giant valley-Zeeman coupling in the surface layer of an intercalated transition metal dichalcogenide. *Nat. Mater.* **22**, 459–465 (2023).
13. Zhang, H.-T. et al. Reconfigurable perovskite nickelate electronics for artificial intelligence. *Science* **375**, 533–539 (2022).
14. Burdett, J. K. & Eisenstein, O. From three- to four-coordination in copper(I) and silver(I). *Inorg. Chem.* **31**, 1758–1762 (1992).
15. Ma, J. & Wei, S.-H. Origin of novel diffusions of Cu and Ag in semiconductors: the case of CdTe. *Phys. Rev. Lett.* **110**, 235901 (2013).
16. Peng, J. et al. Stoichiometric two-dimensional non-van der Waals $AgCrS_2$ with superionic behaviour at room temperature. *Nat. Chem.* **13**, 1235–1240 (2021).
17. Rettie, A. J. E. et al. A two-dimensional type I superionic conductor. *Nat. Mater.* **20**, 1683–1688 (2021).
18. Niedziela, J. L. et al. Selective breakdown of phonon quasiparticles across superionic transition in $CuCrSe_2$. *Nat. Phys.* **15**, 73–78 (2019).
19. Zhong, T., Li, X., Wu, M. & Liu, J.-M. Room-temperature multiferroicity and diversified magnetoelectric couplings in 2D materials. *Natl Sci. Rev.* **7**, 373–380 (2020).
20. Damay, F. et al. Magnetoelastic coupling and unconventional magnetic ordering in the multiferroic triangular lattice $AgCrS_2$. *Phys. Rev. B* **83**, 184413 (2011).
21. Peng, J. et al. Even–odd-layer-dependent ferromagnetism in 2D non-van-der-Waals $CrCuSe_2$. *Adv. Mater.* **35**, 2209365 (2023).
22. Pang, C. et al. High-performance inorganically connected $CuInSe_2$ nanocrystal thin-film transistors and integrated circuits based on the solution process of colloidal synthesis, ligand exchange, and surface treatment. *Chem. Mater.* **33**, 8775–8785 (2021).
23. Harikesh, P. C. et al. Cubic $NaSbS_2$ as an ionic–electronic coupled semiconductor for switchable photovoltaic and neuromorphic device applications. *Adv. Mater.* **32**, 1906976 (2020).
24. Xu, X. et al. High-T_C two-dimensional ferroelectric $CuCrS_2$ grown *via* chemical vapor deposition. *ACS Nano* **16**, 8141–8149 (2022).
25. Sun, L. et al. Chemical vapour deposition. *Nat. Rev. Methods Prim.* **1**, 5 (2021).
26. Zhu, J. et al. Low-thermal-budget synthesis of monolayer molybdenum disulfide for silicon back-end-of-line integration on a 200 mm platform. *Nat. Nanotechnol.* **18**, 456–463 (2023).
27. Zhou, J. et al. Composition and phase engineering of metal chalcogenides and phosphorous chalcogenides. *Nat. Mater.* **22**, 450–458 (2022).
28. Zhang, P. et al. Flux-assisted growth of atomically thin materials. *Nat. Synth.* **1**, 864–872 (2022).
29. Zhou, Z. et al. Stack growth of wafer-scale van der Waals superconductor heterostructures. *Nature* **621**, 499–505 (2023).
30. Li, J. et al. General synthesis of two-dimensional van der Waals heterostructure arrays. *Nature* **579**, 368–374 (2020).
31. Liu, L. et al. Uniform nucleation and epitaxy of bilayer molybdenum disulfide on sapphire. *Nature* **605**, 69–75 (2022).
32. Fu, J.-H. et al. Oriented lateral growth of two-dimensional materials on c-plane sapphire. *Nat. Nanotechnol.* **18**, 1289–1294 (2023).
33. Wang, J. et al. Dual-coupling-guided epitaxial growth of wafer-scale single-crystal WS_2 monolayer on vicinal a-plane sapphire. *Nat. Nanotechnol.* **17**, 33–38 (2022).
34. Xia, Y. et al. 12-inch growth of uniform MoS_2 monolayer for integrated circuit manufacture. *Nat. Mater.* **22**, 1324–1331 (2023).
35. Jain, A. et al. Commentary: The materials project: a materials genome approach to accelerating materials innovation. *APL Mater.* **1**, 011002 (2013).
36. Wu, Q. et al. Resolidified chalcogen precursors for high-quality 2D semiconductor growth. *Angew. Chem. Int. Ed.* **62**, e202301501 (2023).
37. Li, B. et al. Liquid-like thermal conduction in intercalated layered crystalline solids. *Nat. Mater.* **17**, 226–230 (2018).
38. Takahashi, H. et al. Spin-orbit-derived giant magnetoresistance in a layered magnetic semiconductor $AgCrSe_2$. *Phys. Rev. Mater.* **6**, 054602 (2022).
39. Shiomi, Y., Akiba, T., Takahashi, H. & Ishiwata, S. Giant piezoelectric response in superionic polar semiconductor. *Adv. Electron. Mater.* **4**, 1800174 (2018).
40. Peng, J. et al. Fast lithium ion conductivity in layered (li-Ag)CrS_2. *J. Am. Chem. Soc.* **142**, 18645–18651 (2020).
41. Yin, Y.-C. et al. A $LaCl_3$-based lithium superionic conductor compatible with lithium metal. *Nature* **616**, 77–83 (2023).
42. Jun, K. et al. Lithium superionic conductors with corner-sharing frameworks. *Nat. Mater.* **21**, 924–931 (2022).

43. Tanaka, Y. et al. New oxyhalide solid electrolytes with high lithium ionic conductivity > 10 mS cm^{-1} for all-solid-state batteries. *Angew. Chem. Int. Ed.* **62**, e202217581 (2023).
44. Huang, W. et al. Anomalously high ionic conductivity of Li_2SiS_3-type conductors. *J. Am. Chem. Soc.* **144**, 4989–4994 (2022).
45. Canepa, P. et al. High magnesium mobility in ternary spinel chalcogenides. *Nat. Commun.* **8**, 1759 (2017).
46. Zhang, Z. et al. $Na_{11}Sn_2PS_{12}$: a new solid state sodium superionic conductor. *Energy Environ. Sci.* **11**, 87–93 (2018).
47. Brehm, J. A. et al. Tunable quadruple-well ferroelectric van der Waals crystals. *Nat. Mater.* **19**, 43–48 (2020).
48. Gong, Y. et al. Spatially controlled doping of two-dimensional SnS_2 through intercalation for electronics. *Nat. Nanotechnol.* **13**, 294–299 (2018).
49. Yang, Y. et al. 2D layered materials for fast-charging lithium-ion battery anodes. *Small* **19**, 2301574 (2023).
50. Yu, J. et al. Simultaneously ultrafast and robust two-dimensional flash memory devices based on phase-engineered edge contacts. *Nat. Commun.* **14**, 5662 (2023).
51. Pi, L. et al. Broadband convolutional processing using band-alignment-tunable heterostructures. *Nat. Electron.* **5**, 248–254 (2022).
52. Menter, F. R., Kuntz, M. & Langtry, R. Ten years of industrial experience with the SST turbulence model. *Turbul. Heat. Mass Transf.* **4**, 625–632 (2003).
53. Kresse, G. & Furthmüller, J. Efficiency of ab-initio total energy calculations for metals and semiconductors using a plane-wave basis set. *Comput. Mater. Sci.* **6**, 15–50 (1996).
54. Blöchl, P. E. Projector augmented-wave method. *Phys. Rev. B* **50**, 17953–17979 (1994).
55. Perdew, J. P. et al. Atoms, molecules, solids, and surfaces: applications of the generalized gradient approximation for exchange and correlation. *Phys. Rev. B* **46**, 6671–6687 (1992).
56. Henkelman, G., Uberuaga, B. P. & Jónsson, H. A climbing image nudged elastic band method for finding saddle points and minimum energy paths. *J. Chem. Phys.* **113**, 9901–9904 (2000).

Acknowledgements

This work was supported by the National Natural Science Foundation of China (52322210, 22375069, 52172144, and U21A2069), the National Key Research and Development Program of China (2021YFA1200500), and the Innovation Project of Optics Valley Laboratory (OVL2023PY007). Here, the authors also thank the technical support from the Analytical and Testing Center at Huazhong University of Science and Technology.

Author contributions

X.Z., T.Z., and X.X. conceived and designed the experiments. X.X. and Y.C. synthesized the materials. X.X., P.L., Y.C., and D.L. performed the AFM, Raman, and SHG characterizations of the samples. X.X. and H.L. performed the HRTEM and HAADF-STEM characterizations and worked on the analysis of the results. X.X. performed the electrochemical impedance measurements. X.X., P.L., Y.C., H.W., and X.S. performed device fabrication and measurement. X.X. and Z.L. performed the PFM measurements. X.X. and Y.C. wrote the paper with inputs from T.Z., X.Z., and J.W. All authors participated in discussions and approved the manuscript.

Competing interests

The authors declare no competing interests.

Additional information

Supplementary information The online version contains supplementary material available at https://doi.org/10.1038/s41467-024-48690-7.

Correspondence and requests for materials should be addressed to Xing Zhou or Tianyou Zhai.

Peer review information *Nature Communications* thanks Xidong Duan, Wei-jin Hu and Jing Peng for their contribution to the peer review of this work. A peer review file is available.